Received: Added at production | Revised: Added at production | Accepted: Added at production

DOI: xxx/xxxx

ARTICLE TYPE

Robust Flat-Facet Triangular Shell Finite Element

Petr Krysl*

[1]Structural Engineering Department, University of California, San Diego, California, USA

Correspondence
*Petr Krysl. Email: pkrysl@ucsd.edu

Summary

A flat facet finite element with three nodes and six degrees of freedom per node for linear static and dynamic analysis of thick and thin shells is presented. The membrane response is modeled with constant strain triangles. The bending response treats the transverse shear with an improved version of the discrete-shear-gap technique. The main novelty of the present approach is the robust treatment of the drilling rotations: the element internally responds to five degrees of freedom per node, but externally it naturally possesses six degrees of freedom per node. The drilling degree of freedom is decoupled from the bending and twisting, and the undesirable user-selectable arbitrary stabilization is avoided. The element is shown to be robust for extremely thin shells, and passes tests such as the Raasch hook problem. Performance is illustrated with static and dynamic examples including branched and folded shells.

KEYWORDS:
flat facet shell finite element, discrete shear gap, drilling rotation, branched shells, folded shells

Draft: as submitted for review, December 2021

INTRODUCTION

Structures advantageously modeled with shells are widely encountered in the civil and marine engineering, aerospace, aeronautical and automobile industries. The formulations of shell finite elements are quite complex compared to other structural elements. Over the past several decades, many hundreds of papers have appeared on the subject of shell finite element analysis, and the search for a formulation that possesses all the desirable characteristics (robustness, low sensitivity to poorly-shaped meshes, low computational cost) is still on [1,2,3].

Today, the literature on modeling of shells would require an entire article for a reasonably complete coverage. We shall not attempt to sort through this literature here; rather we shall refer to older [4,5] and recent [6,7] reviews.

The most appealing characteristic of shell structures is the ability of using material efficiently by developing membrane stresses due to the curvature of the shell. So curved surfaces seem to be an inherent characteristic of structures modeled as shells. Nevertheless, shells can be profitably modeled with flat facet finite element meshes, as such flat facet elements tend to be rather simple to formulate and efficient in large scale computations [8].

The modelling of a general shell of complex geometry and topology derives substantial advantage from the use of triangular element shapes. The simplest triangular flat shell finite element combines the constant strain triangle for membrane action with some suitable plate element for bending action. The difficulty is how to manage locking: In many applications, it is necessary to include transverse shear deformations, which play an important role for the case of thick shells and layered (sandwich) thin shells. Transverse shear is accounted for by making use of the Mindlin-Reissner shell theory, often referred to as “first order theory”, which involves a constant through-the-thickness transverse shear distribution. It is well known that displacement based Mindlin-Reissner shell elements often exhibit shear locking when elements become thin. Here we shall take advantage of the recent developments of the discrete shear gap technique [9].

Another issue that faces developers of simple facet elements is how to handle drilling rotations: rotations about the "normal" to the shell surface. Some formulations opt for adding drilling rotation degrees of freedom at various levels [10,11,12,3] (theory, discrete model), others prefer to get rid of rotations altogether [13,14]. We elect to transform the drilling rotations out at the element level, while keeping them in the assembled global system of balance equations. This is useful from a couple of viewpoints: The formulation is quite robust, passing all currently known challenging benchmarks, and also it is directly applicable to folded and branched shells without any additional devices.

Finally, a good selling point for finite element technologies has always been a low cost of processing of the discrete model: the faster, the better. The present formulation is so simple that a single integration point, which for a three-node triangle really amounts to essentially analytically derived expressions, is quite sufficient. Hence, the present elements can be processed very efficiently.

The plan for the current article is to briefly review the formulation of the membrane and bending/transverse shear response in Section 1. The development is straightforward, and for the most part well known, but we do add a twist by making the transverse shear response of the element isotropic, which is an improvement on the original idea. We propose in fact two ways: averaging of the strains, and averaging of the transverse-shear stiffness matrix.

Section 2 is where the novelty of the present approach lies: we develop a transformation between the global degrees of freedom, where the nodes carry six degrees of freedom, three translations and three rotations, and the element level, where the drilling rotation has no physical meaning, and the element responds to three translations and two flexural rotations. The transformation is enabled by establishing approximate or exact normals at the nodes, where possible; creases or junctions of shell branches are excepted. The transformation leaves the drilling degrees of freedom on the global level entirely decoupled from each other and from the other degrees of freedom. Therefore, we totally eliminate the dependence on an arbitrary parameter, which plagued the previous ad hoc approaches. We study various aspects of the technique, such as the effect of boundary conditions, the treatment of creases and junctions of multiple shells, and use of the element in dynamic simulations.

The properties of the present formulation are highlighted on a number of challenging benchmarks in Section 3. We study a folded-shell benchmark, a clamped hyperbolic paraboloid shell, a hyperboloid of revolution, both membrane- and bending-dominated, and we illustrate both the accuracy and the performance of the present formulation on an example of industrial-scale free-vibration analysis. Finally, in the Conclusions we offer some remarks on potential future extensions.

1 | ELASTIC PROPERTIES OF THE ELEMENT IN ITS FRAME

1.1 | Element cartesian frame basis vectors

Our formulation is based on the three-node linear triangle. As shown in Figure 1, the element carries a frame (basis) attached at its centroid, defined by the two nodes 1 and 2 which determine the direction of the local x axis. The normal is obviously determined by the plane of the triangle. The two coordinates given by the basis vectors $\mathbf{E}_1$ and $\mathbf{E}_2$ are referred to as x_1 and x_2. The elastic and inertial properties of the flat facet shell element are entirely expressed in this local element basis.

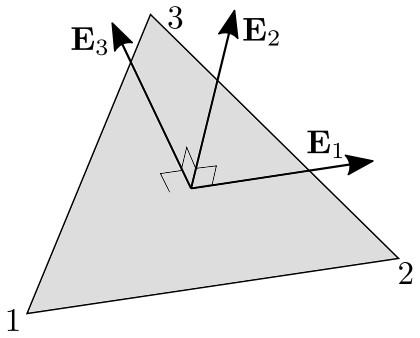

FIGURE 1 Element cartesian frame, $\mathbf{E}_j$.

We write

$$[Q]_B \tag{1}$$

to indicate that the quantity Q is expressed on the cartesian basis $\mathbf{B}$. In this work we formulate the global degrees of freedom in the global cartesian basis

$$[\mathbf{G}]_G = \left[\left[\mathbf{G}_1\right]_G, \left[\mathbf{G}_2\right]_G, \left[\mathbf{G}_3\right]_G\right] = [\mathbf{1}] \ , \tag{2}$$

where $\mathbf{G}_j$ is the j-th basis vector. The matrix of the components of the basis vectors expressed on the $\mathbf{G}$ basis yields the identity matrix.

The element-attached basis $\mathbf{E}$ is expressed in the global cartesian basis $\mathbf{G}$ as

$$[\mathbf{E}]_G = \left[\left[\mathbf{E}_1\right]_G, \left[\mathbf{E}_2\right]_G, \left[\mathbf{E}_3\right]_G\right] \ . \tag{3}$$

Here $\left[\mathbf{E}_3\right]_G$ is the normal to the element surface expressed on the global cartesian basis $\mathbf{G}$. (Refer to Figure 1.)

1.2 | Degrees of freedom

We assume three translations and three rotations per node, so that the degrees of freedom of the triangle are

$$\begin{bmatrix} \left[{}^1\mathbf{q}\right]_E \\ \left[{}^2\mathbf{q}\right]_E \\ \left[{}^3\mathbf{q}\right]_E \end{bmatrix} , \tag{4}$$

where the nodal degrees of freedom consist of displacements $\mathbf{d}$ and rotations $\mathbf{r}$

$$\left[{}^k\mathbf{q}\right]_E = \begin{bmatrix} \left[{}^k\mathbf{d}\right]_E \\ \left[{}^k\mathbf{r}\right]_E \end{bmatrix} \ . \tag{5}$$

The rotation components are described with the right hand side rule: positive when turning about the axis with the thumb pointing along the axis, and the fingers describing the turning direction. The rotation $\left[{}^k\mathbf{r}_3\right]_E = \left[{}^k\theta_3\right]_E$, the so called drilling degree of freedom, is not associated with any stiffness at the element level. That calls for a special treatment, presented in Section 2.

1.3 | Membrane action

The membrane strains can be computed as

$$[\boldsymbol{\epsilon}]_E = \sum_k \left[\ {}^k\mathbf{B}^m\right]_E \left[{}^k\mathbf{q}\right]_E \ . \tag{6}$$

Here the membrane strain-displacement matrix for node k reads

$$\left[{}^k\mathbf{B}^m\right]_E = \begin{bmatrix} \partial\, {}^kN/\partial x_1 & 0 & 0\ 0\ 0\ 0 \\ 0 & \partial\, {}^kN/\partial x_2 & 0\ 0\ 0\ 0 \\ \partial\, {}^kN/\partial x_2 & \partial\, {}^kN/\partial x_1 & 0\ 0\ 0\ 0 \end{bmatrix}_E , \tag{7}$$

where ${}^kN$ is the basis function associated with node k. Note that the basis functions are expressed on the element basis $\mathbf{E}$. The membrane stiffness of the triangle is then computed with a single-point quadrature as

$$\left[\mathbf{K}^m\right]_E = A \left[\mathbf{B}^m\right]_E^T \left[\mathbf{D}^m\right]_E \left[\mathbf{B}^m\right]_E \ , \tag{8}$$

where $[\mathbf{D}^m]_E$ is the membrane stiffness of the shell, which in the case of an homogeneous material reads

$$\left[\mathbf{D}^m\right]_E = t \left[\mathbf{D}^p\right]_E \ . \tag{9}$$

Here t is the thickness of the shell, and $[\mathbf{D}^p]_E$ is the plane-stress material stiffness matrix, which for an isotropic material reads

$$\left[\mathbf{D}^p\right]_E = \frac{E}{1-\nu^2} \begin{bmatrix} 1 & \nu & 0 \\ \nu & 1 & 0 \\ 0 & 0 & \dfrac{1}{2(1+\nu)} \end{bmatrix}_E \ . \tag{10}$$

Above E and ν are the Young's modulus and the Poisson ratio. The 3×18 matrix $[\mathbf{B}^m]_E$ aggregates the nodal strain-displacement matrices

$$\left[\mathbf{B}^m\right]_E = \left[\ \left[\ {}^1\mathbf{B}^m\right]_E \ , \left[\ {}^2\mathbf{B}^m\right]_E \ , \left[\ {}^3\mathbf{B}^m\right]_E \ \right] \ . \tag{11}$$

1.4 | Flexural action

The curvatures due to bending can be computed as

$$[\boldsymbol{\kappa}]_E = \sum_k \left[{}^k\mathbf{B}^b \right]_E \left[{}^k\mathbf{q} \right]_E \tag{12}$$

Here the curvature-displacement matrix for node k reads

$$\left[{}^k\mathbf{B}^b \right]_E = \begin{bmatrix} 0 & 0 & 0 & 0 & \partial\, {}^kN/\partial x_1 & 0 \\ 0 & 0 & 0 & -\partial\, {}^kN/\partial x_2 & 0 & 0 \\ 0 & 0 & 0 & -\partial\, {}^kN/\partial x_1 & \partial\, {}^kN/\partial x_2 & 0 \end{bmatrix} . \tag{13}$$

The bending stiffness of the triangle is then computed with a single-point quadrature as

$$\left[\mathbf{K}^b \right]_E = A \left[\mathbf{B}^b \right]_E^T \left[\mathbf{D}^b \right]_E \left[\mathbf{B}^b \right]_E , \tag{14}$$

where $\left[\mathbf{D}^b \right]_E$ is the bending stiffness matrix of the shell. For an isotropic material

$$\left[\mathbf{D}^b \right]_E = \frac{t^3}{12} \left[\mathbf{D}^p \right]_E , \tag{15}$$

where the plane stress material stiffness matrix $[\mathbf{D}^p]_E$ was given in (10). The matrix $\left[\mathbf{B}^b \right]_E$ aggregates the nodal curvature-displacement matrices

$$\left[\mathbf{B}^b \right]_E = \left[\left[{}^1\mathbf{B}^b \right]_E , \left[{}^2\mathbf{B}^b \right]_E , \left[{}^3\mathbf{B}^b \right]_E \right] . \tag{16}$$

1.5 | Transverse shear action

We adopt a modification of the Discrete Shear Gap (DSG) approach[9]. The central idea of DSG is to compute the so called shear gaps as the line integrals of the shear strains along the coordinate lines in the element reference domain, i.e. in between the nodes. Then the shear strain is obtained by differentiating the shear gap obtained as interpolation of the shear gaps at the nodes using the finite element basis functions. The nodal shear strain-displacement matrices have been for the flat triangle derived explicitly in the original publication[9], but our notation and sign convention for the rotations is different and hence we prefer to draw on the matrices published in Reference 15: node 1

$$\left[{}^1\mathbf{B}^s \right]_E = \frac{1}{2A} \begin{bmatrix} 0, & 0, & b-d, & 0, & A, & 0 \\ 0, & 0, & c-a, & -A, & 0, & 0 \end{bmatrix} , \tag{17}$$

node 2,

$$\left[{}^2\mathbf{B}^s \right]_E = \frac{1}{2A} \begin{bmatrix} 0, & 0, & d, & (-bd)/2, & (ad)/2, & 0 \\ 0, & 0, & -c, & (bc)/2, & (-ac)/2, & 0 \end{bmatrix} , \tag{18}$$

and, node 3

$$\left[{}^3\mathbf{B}^s \right]_E = \frac{1}{2A} \begin{bmatrix} 0, & 0, & -b, & (bd)/2, & (-bc)/2, & 0 \\ 0, & 0, & a, & (-ad)/2, & (ac)/2, & 0 \end{bmatrix} . \tag{19}$$

Here A is the element area, $a = {}^2x_1 - {}^1x_1$, $b = {}^2x_2 - {}^1x_2$, $c = {}^3x_1 - {}^1x_1$, $d = {}^3x_2 - {}^1x_2$. The transverse shear strains are then computed as

$$\left[\boldsymbol{\gamma} \right]_E = \sum_k \left[{}^k\mathbf{B}^s \right]_E \left[{}^k\mathbf{q} \right]_E , \tag{20}$$

or,

$$\left[\boldsymbol{\gamma} \right]_E = \left[\mathbf{B}^s \right]_E \left[{}^k\mathbf{q} \right]_E . \tag{21}$$

In the original publication, the dependence of the results on the numbering (ordering) of the element nodes was noted[9]. Even though it is not a major obstacle to convergence, an "isotropic response" of the element would be preferred. Cell-based smoothing of the shear strains was proposed by Nguyen-Thoi et al.[16] as a means of making the transverse shear strain formulation isotropic. The net effect of the smoothing is simply averaging of the shear strain-displacement matrices for three different orientations of the triangle. Let us denote $o_1 = (1, 2, 3)$, $o_2 = (2, 3, 1)$, and $o_3 = (3, 1, 2)$ the three possible orderings in which the three nodes of a triangle can be taken. Then the shear strain-displacement matrices may be calculated as the averages

$$\left[{}^k\widetilde{\mathbf{B}}^s \right]_E = \frac{1}{3} \sum_{j=1}^{3} \left[{}^k\mathbf{B}^s_{o_j} \right]_E , \tag{22}$$

where by $\left[{}^{k}\mathbf{B}^{s}_{o_j}\right]_E$ we mean each of the three matrices (17)-(19) for a given k computed for the ordering of the nodes o_j. Note that computing the matrix $\left[{}^{k}\mathbf{B}^{s}_{o_j}\right]_E$ for a particular ordering of the nodes means the parameters a, b, c and d must be recomputed according to the reordered coordinates of the nodes. Computing the transverse shear strains from

$$\left[\boldsymbol{\gamma}\right]_E = \sum_k \left[\,{}^{k}\widetilde{\mathbf{B}}^{s}\right]_E \left[{}^{k}\mathbf{q}\right]_E \tag{23}$$

then leads to an isotropic response (i.e. the shear response does not depend on the ordering of the nodes).

A seemingly unrelated technique was presented by Cui and Tian[17]: the shear gaps were calculated from the centroid of the triangle towards the nodes. The deflection at the centroid was taken as the average of the nodal deflections. However, the ultimate result of that approach is again averaging of the transverse shear-displacement matrices over the three node orderings, i.e. equation (22).

The isotropic shear stiffness matrix can then be evaluated (with a single-point quadrature, since all integrands are constant) as

$$\left[\mathbf{K}^s\right]_E = A \left[\widetilde{\mathbf{B}}^s\right]_E^T \left[\mathbf{D}^s\right]_E \left[\widetilde{\mathbf{B}}^s\right]_E \tag{24}$$

were $[\mathbf{D}^s]_E$ is the transverse shear stiffness of the shell, described below. The matrix $\left[\widetilde{\mathbf{B}}^s\right]_E$ aggregates the averaged nodal strain-displacement matrices

$$\left[\widetilde{\mathbf{B}}^s\right]_E = \left[\left[\,{}^{1}\widetilde{\mathbf{B}}^s\right]_E, \left[\,{}^{2}\widetilde{\mathbf{B}}^s\right]_E, \left[\,{}^{3}\widetilde{\mathbf{B}}^s\right]_E\right] . \tag{25}$$

We can refer to the transverse shear stiffness matrix (24) as the **averaged-B** formulation.

An alternative to the averaging of the transverse strain-displacement matrix has already been suggested by Talaslidis and Wempner[18], where the energy of the transverse shear strains was averaged (their equation (46a,b)) in order to achieve isotropic response. Therefore, the alternative formulation would calculate the contribution of the transverse shear strain to the stiffness matrix as

$$\left[\mathbf{K}^s\right]_E = \frac{A}{3} \sum_{j=1}^{3} \left[\mathbf{B}^s_{o_j}\right]_E^T \left[\mathbf{D}^s\right]_E \left[\mathbf{B}^s_{o_j}\right]_E . \tag{26}$$

The matrix $[\mathbf{B}^s]_E$ aggregates the nodal strain-displacement matrices

$$\left[\mathbf{B}^s_{o_j}\right]_E = \left[\left[\,{}^{1}\mathbf{B}^s_{o_j}\right]_E, \left[\,{}^{2}\mathbf{B}^s_{o_j}\right]_E, \left[\,{}^{3}\mathbf{B}^s_{o_j}\right]_E\right] . \tag{27}$$

We can refer to the transverse shear stiffness matrix (26) as the **averaged-K** formulation.

The transverse shear stiffness matrix of the shell can be described for an isotropic homogeneous material as

$$\left[\mathbf{D}^s\right]_E = \psi \frac{Et}{2(1+\nu)} \begin{bmatrix} 1 & 0 \\ 0 & 1 \end{bmatrix}_E . \tag{28}$$

Here we have introduced the correction factor ψ which incorporates the modification of the stiffness due to the non-uniform distribution of the shear stress through the thickness $\kappa = 5/6$, and also improves the response for coarse meshes à la Lyly et al.[19] and Bischoff and Bletzinger[20]

$$\psi = \kappa \frac{t^2}{t^2 + \alpha h^2} , \tag{29}$$

where we can take $\alpha = \kappa/(2(1+\nu))$ as recommended in Reference 20. Here h can be taken as $\sqrt{2}\times$ the square root of the area of the triangle as a measure of the length of the element edges.

1.6 | Properties of the elementwise stiffness matrix

The overall stiffness matrix of the element in the local element coordinates is obviously

$$[\mathbf{K}]_E = \left[\mathbf{K}^m\right]_E + \left[\mathbf{K}^b\right]_E + \left[\mathbf{K}^s\right]_E . \tag{30}$$

This stiffness matrix has a rank of 8: it has six rigid body modes, one higher order torsional mode[18], and three zero energy modes due to the drilling rotations being associated with no stiffness.

The torsional mode corresponds to the rotation of the bottom surface of the shell relative to the top surface about the normal to the element surface. The torsional mode is uncoupled from the flexural modes[18], and it is incommunicable in meshes of more than two connected triangles.

The drilling rotation degrees of freedom will be treated in the next section, and we will be able to show that singularities of the stiffness due to those effects have been cured. The element transformations will lead to a proper-rank global stiffness matrix.

2 | HANDLING OF THE DRILLING ROTATIONS

The drilling degree of freedom on the element basis is not associated with any stiffness. Without further intervention, this would lead to trouble: The global stiffness would be singular whenever all elements connected to a node were co-planar, and the global stiffness would be nearly singular for curved shells, where at some node the drilling degree of freedom in one element had a nonzero, but only small, component in the direction of a bending degree of freedom in another element. There are essentially two ways in which the **potential-singularity problem** has been addressed in the literature (refer to the review in Reference 4): The potential singularity may be treated at the element level, or at the global system level.

The **element-level approach** would revise the mechanical formulation to incorporate rotations about the normal to the surface of the element. These rotations may be associated with real stiffness[11,10], or with a fictitious stiffness[21,22]. In either method, there may be user-tunable parameters upon which the accuracy or stability would depend. That is a problem: If the drilling rotation was coupled to the bending action, an excessive stiffness in the membrane drilling rotation would deleteriously affect inextensible bending[23]. On the other hand, too small of a drilling stiffness would destroy the condition number of the stiffness matrix. Recently, some advances have been reported that reduced or eliminated the dependence of the solution on the drilling stiffness parameters[22,12].

The second, **global approach** attempts to treat the drilling degrees of freedom in the assembled system of equations[24]. One possibility is to introduce constraints applied to singular degrees of freedom upon detection of zero pivots. The stiffness matrix may also be analyzed for nearly zero singular values of rotation-related diagonal sub matrices of the global stiffness matrix. In either case, the analysis of the assembled system is not nearly robust enough.

In addition to the potential singularity, there is also a second issue: for shear-flexible shells, the **transfer of the twisting moments** between elements may end up coupled to the drilling rotations[24]. As a manifestation, the shell element formulation would fail one of the known shell benchmarks, the Raasch hook problem[25,24,26]: The structure consists of two strips of circular arcs which are responding to a transverse load by torsion. Consequently, the transfer of twisting moments from element to element is crucial, and shear-flexible shell element formulations are known to diverge from the correct deflection[25,27] due to uncontrolled spurious transverse shear[24].

In particular, consider what happens if we proceed by computing the global element stiffness matrix by the commonly-applied global-to-element transformation of basis

$$[\mathbf{K}]_G = [\mathbf{T}]_G^T [\mathbf{K}]_E [\mathbf{T}]_G \ , \tag{31}$$

where $[\mathbf{T}]_G$ is the transformation matrix, constructed from the rotation matrices $[\mathbf{E}]_G$

$$[\mathbf{T}]_G = \begin{bmatrix} [\mathbf{E}]_G^T & \mathbf{0} & \mathbf{0} & \mathbf{0} & \mathbf{0} & \mathbf{0} \\ \mathbf{0} & [\mathbf{E}]_G^T & \mathbf{0} & \mathbf{0} & \mathbf{0} & \mathbf{0} \\ \mathbf{0} & \mathbf{0} & [\mathbf{E}]_G^T & \mathbf{0} & \mathbf{0} & \mathbf{0} \\ \mathbf{0} & \mathbf{0} & \mathbf{0} & [\mathbf{E}]_G^T & \mathbf{0} & \mathbf{0} \\ \mathbf{0} & \mathbf{0} & \mathbf{0} & \mathbf{0} & [\mathbf{E}]_G^T & \mathbf{0} \\ \mathbf{0} & \mathbf{0} & \mathbf{0} & \mathbf{0} & \mathbf{0} & [\mathbf{E}]_G^T \end{bmatrix}_G . \tag{32}$$

This naive approach would result in a divergence in the Raasch hook problem, and adding artificial drilling stiffness at the element level would not help at all.

2.1 | Transformations to achieve robust response

Our approach is an element-level treatment:

1. Firstly we design a transformation from the element basis to a nodal basis. The transformation is formulated to isolate the drilling degree of freedom from the bending degrees of freedom, and to support proper transfer of twisting moments.

2. Secondly we apply artificial springs to the drilling degrees of freedom which are now separated from the other degrees of freedom.

Our approach is related to the treatment of Reference 24. We will first describe our own formulation, and then we will relate it to the developments of Reference 24.

We begin by introducing, in addition to the global and element basis, a third basis which is defined at each node. For the moment, we shall assume that the surface of the shell consists of one **smooth face without creases**. We shall generalize this idea below to surfaces with creases and to surfaces with junctions of two or more shell faces.

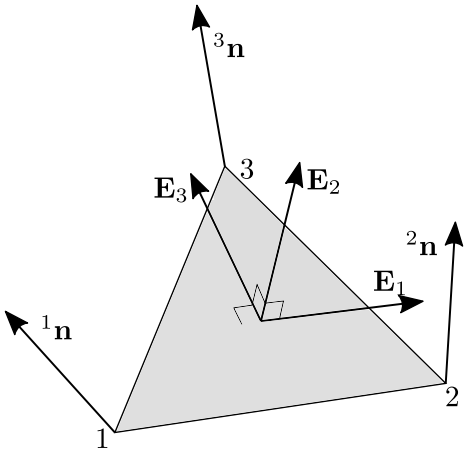

FIGURE 2 Nodal normals. Each node has its own normal, which in general is different from the normal to the element surface for each element connected to the node.

First we construct the nodal normals. The vectors that we refer to as normals need not be actually normal to the surface of the shell at the node. We only require that all elements connected to a node agree on this "normal" direction, which should be a decent approximation to the true normal.

We can calculate the normals from the approximation of the actual surface of the shell by its triangulation: Node k is then associated with "normal" $\left[{}^k\mathbf{n}\right]_G$, which is a weighted average of the normals of the elements connected at the node. Alternatively, the true nodal normals may be given analytically for special surfaces, such as spheres, cylinders, etc. Figure 2 shows that the normals at the nodes will in general be different from the normals to the elements connected at the node.

Then, when processing any given shell finite element, Cartesian coordinate basis ${}^k\mathbf{A}$ is constructed for each of the three nodes of the element such that the basis vector $\left[{}^k\mathbf{A}_3\right]_E$ at node k coincides with the normal at the node k: $\left[{}^k\mathbf{A}_3\right]_E = \left[{}^k\mathbf{n}\right]_E = [\mathbf{E}]_G^T \left[{}^k\mathbf{n}\right]_G$. (Refer to Figure 2.) The remaining Cartesian basis vectors of the nodal basis are obtained by rotating the element frame $[\mathbf{E}]_E = [\mathbf{1}]$ through the angle ϕ subtended by $\left[{}^k\mathbf{n}\right]_E$ and $\left[\mathbf{E}_3\right]_E$. (Refer to Figure 3.) Hence, the vectors $\left[{}^k\mathbf{A}_1\right]_E$ and $\left[{}^k\mathbf{A}_2\right]_E$ are obtained from $\left[\mathbf{E}_1\right]_E$ and $\left[\mathbf{E}_2\right]_E$ by rotating through the rotation vector $\boldsymbol{\phi} = \left[\mathbf{E}_3\right]_E \times \left[{}^k\mathbf{A}_3\right]_E$, i.e.

$$\left[{}^k\mathbf{A}_j\right]_E = \left[\exp\left(\boldsymbol{\phi}\right)\right]_E \left[\mathbf{E}_j\right]_E \ . \tag{33}$$

As a result, each element has three bases defined at its nodes, in general different for each node k

$$\left[{}^k\mathbf{A}\right]_E = \left[{}^k\left[\mathbf{A}_1\right]_E, {}^k\left[\mathbf{A}_2\right]_E, {}^k\left[\mathbf{A}_3\right]_E\right] \ . \tag{34}$$

Each element connected to a given node will compute for this node a different set of basis vectors (34). These different bases will only agree on the direction of the third vector, ${}^k\mathbf{A}_3 = {}^k\mathbf{n}$.

At this point we will focus on the transformation of the rotations between the element basis and the node basis at a fixed node k of the triangle (1, 2, or 3). Hence, we will omit the designation ${}^k\mathbf{A}$ for the nodal transformation matrix, and we will write simply $\mathbf{A}$.

At first sight, the relationship between physical rotations in the element basis $\mathbf{E}$ and the rotations on the nodal basis $\mathbf{A}$ may be written as

$$\begin{bmatrix} \theta_1 \\ \theta_2 \\ \theta_3 \end{bmatrix}_E = [\mathbf{A}]_E \, [\boldsymbol{\theta}]_A \ . \tag{35}$$

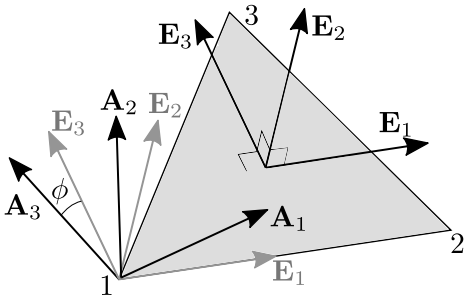

FIGURE 3 Nodal cartesian basis produced by rotation of the element basis so that the rotated element normal coincides with the nodal normal.

Alas, the rotation $\left[\theta_3\right]_E$ has no mechanical meaning: there is no stiffness associated with this rotation. The numerical magnitude of this rotation is arbitrary, due to the lack of mechanical meaning, but we set this to zero for definiteness, $\left[\theta_3\right]_E = 0$.

However, it is useful to have in the formulation a meaningful definition of the drilling rotation. Hence, we supplement the useless nodal rotation about the normal to the element $\left[\theta_3\right]_E$ with the continuum rotation α_3

$$\alpha_3 = \frac{1}{2}\left(\frac{\partial u_2}{\partial x_1} - \frac{\partial u_1}{\partial x_2}\right) , \tag{36}$$

where all the quantities in this equation are on the element frame **E**. And so we write the transformation between the rotations in the element basis **E** and the rotations on the nodal basis **A** as

$$\begin{bmatrix} \theta_1 \\ \theta_2 \\ \theta_3 + \alpha_3 \end{bmatrix}_E = \begin{bmatrix} \theta_1 \\ \theta_2 \\ \alpha_3 \end{bmatrix}_E = [\mathbf{A}]_E \, [\boldsymbol{\theta}]_A \ . \tag{37}$$

The last of the three equations of this transformation can be written as

$$\left[\,\alpha_3\,\right]_E = \left[\mathbf{A}_{3,1:2}\right]_E \begin{bmatrix} \theta_1 \\ \theta_2 \end{bmatrix}_A + \left[\mathbf{A}_{3,3}\right]_E \left[\,\theta_3\,\right]_A \ , \tag{38}$$

where we use the notation $\left[\mathbf{A}_{3,1:2}\right]_E$ to designate a sub-matrix consisting of the row 3 and the columns 1 and 2 of the matrix $[\mathbf{A}]_E$. The above equation can be solved for the drilling rotation on the nodal basis

$$\left[\,\theta_3\,\right]_A = \left[\mathbf{A}_{3,3}\right]_E^{-1} \left(- \left[\mathbf{A}_{3,1:2}\right]_E \begin{bmatrix} \theta_1 \\ \theta_2 \end{bmatrix}_A + \left[\,\alpha_3\,\right]_E \right) . \tag{39}$$

Now, the first two equations of (37) read

$$\begin{bmatrix} \theta_1 \\ \theta_2 \end{bmatrix}_E = \left[\mathbf{A}_{1:2,1:2}\right]_E \begin{bmatrix} \theta_1 \\ \theta_2 \end{bmatrix}_A + \left[\mathbf{A}_{1:2,3}\right]_E \left[\,\theta_3\,\right]_A \tag{40}$$

which can be rewritten with the aid of (39) as

$$\begin{bmatrix} \theta_1 \\ \theta_2 \end{bmatrix}_E = \left[\mathbf{A}_{1:2,1:2}\right]_E \begin{bmatrix} \theta_1 \\ \theta_2 \end{bmatrix}_A + \left[\mathbf{A}_{1:2,3}\right]_E \left[\mathbf{A}_{3,3}\right]_E^{-1} \left(- \left[\mathbf{A}_{3,1:2}\right]_E \begin{bmatrix} \theta_1 \\ \theta_2 \end{bmatrix}_A + \left[\,\alpha_3\,\right]_E \right) , \tag{41}$$

or, grouping together the terms, as

$$\begin{bmatrix} \theta_1 \\ \theta_2 \end{bmatrix}_E = \left(\left[\mathbf{A}_{1:2,1:2}\right]_E - \left[\mathbf{A}_{3,3}\right]_E^{-1} \left[\mathbf{A}_{1:2,3}\right]_E \left[\mathbf{A}_{3,1:2}\right]_E \right) \begin{bmatrix} \theta_1 \\ \theta_2 \end{bmatrix}_A + \left[\mathbf{A}_{3,3}\right]_E^{-1} \left[\mathbf{A}_{1:2,3}\right]_E \left[\,\alpha_3\,\right]_E \ . \tag{42}$$

Using the usual basis functions of the triangle, ${}^{j}N$, we can express the continuum rotation (36) through the degrees of freedom at the nodes of the triangle

$$\alpha_3 = \frac{1}{2}\left(\sum_j \frac{\partial\, {}^{j}N}{\partial x_1}\, {}^{j}u_2 - \sum_j \frac{\partial\, {}^{j}N}{\partial x_2}\, {}^{j}u_1 \right) . \tag{43}$$

The degrees of freedom (the displacements ${}^{j}u_i$ at the node j in the plane of the triangle in the direction of i), can be calculated from the displacement vectors at the nodes of the triangle, expressed on the nodal basis

$${}^{j}u_i = \left[\mathbf{E}_i\right]_E^T [\mathbf{A}]_E \left[{}^{j}\mathbf{d}\right]_A \ . \tag{44}$$

Here ${}^j\mathbf{d}$ is the vector of displacements at node j. Substituting (44) into (43), and then replacing α_3 with the result in (42) delivers

$$\begin{aligned}\begin{bmatrix}\theta_1\\ \theta_2\end{bmatrix}_E &= \left(\left[\mathbf{A}_{1:2,1:2}\right]_E - \left[\mathbf{A}_{3,3}\right]_E^{-1}\left[\mathbf{A}_{1:2,3}\right]_E\left[\mathbf{A}_{3,1:2}\right]_E\right)\begin{bmatrix}\theta_1\\ \theta_2\end{bmatrix}_A \\ &\quad + \left[\mathbf{A}_{3,3}\right]_E^{-1}\left[\mathbf{A}_{1:2,3}\right]_E\frac{1}{2}\left(\sum_j \frac{\partial\, {}^jN}{\partial x_1}\ \left[\mathbf{E}_2\right]_E^T[\mathbf{A}]_E\left[{}^j\mathbf{d}\right]_A - \sum_j \frac{\partial\, {}^jN}{\partial x_2}\ \left[\mathbf{E}_1\right]_E^T[\mathbf{A}]_E\left[{}^j\mathbf{d}\right]_A\right)\end{aligned} \tag{45}$$

which may be fruitfully simplified as

$$\begin{aligned}\begin{bmatrix}\theta_1\\ \theta_2\end{bmatrix}_E &= \left(\left[\mathbf{A}_{1:2,1:2}\right]_E - \left[\mathbf{A}_{3,3}\right]_E^{-1}\left[\mathbf{A}_{1:2,3}\right]_E\left[\mathbf{A}_{3,1:2}\right]_E\right)\begin{bmatrix}\theta_1\\ \theta_2\end{bmatrix}_A \\ &\quad + \left[\mathbf{A}_{3,3}\right]_E^{-1}\left[\mathbf{A}_{1:2,3}\right]_E\frac{1}{2}\sum_j\left(\frac{\partial\, {}^jN}{\partial x_1}\ \left[\mathbf{E}_2\right]_E^T - \sum_j \frac{\partial\, {}^jN}{\partial x_2}\ \left[\mathbf{E}_1\right]_E^T\right)[\mathbf{A}]_E\left[{}^j\mathbf{d}\right]_A\end{aligned} . \tag{46}$$

The above equation expresses the two rotations in the plane of the element, $\left[\theta_1\right]_E$ and $\left[\theta_2\right]_E$, in terms of the rotations in the nodal basis, $\left[\theta_1\right]_A$ and $\left[\theta_2\right]_A$, and importantly also in terms of the translations of the nodes $\left[{}^j\mathbf{d}\right]_A$. The drilling rotation, $\left[\theta_3\right]_A$, no longer plays any role. The rotation transformation is completed with

$$\left[\,\theta_3\,\right]_E = 0\ . \tag{47}$$

The transformation of the elements stiffness matrix now proceeds in two steps. In the first step, we transform the element stiffness matrix into the nodal basis using the transformation

$$[\mathbf{K}]_A = \left[\mathbf{T}^A\right]_E^T[\mathbf{K}]_E\left[\mathbf{T}^A\right]_E\ . \tag{48}$$

The transformation matrix $\left[\mathbf{T}^A\right]_E$ takes as input a vector in the nodal basis ($\mathbf{A}$) and outputs a vector in the element basis ($\mathbf{E}$). Using the transformation of the rotation degrees of freedom (46) and (47), we construct the 3×3 matrices

$$\left[{}^k\widetilde{\mathbf{A}}\right]_E = \begin{bmatrix}\left[{}^k\mathbf{A}_{1:2,1:2}\right]_E - \left[{}^k\mathbf{A}_{3,3}\right]_E^{-1}\left[{}^k\mathbf{A}_{1:2,3}\right]_E\left[{}^k\mathbf{A}_{3,1:2}\right]_E & , \mathbf{0}\\ \mathbf{0} & , 0\end{bmatrix} \tag{49}$$

and

$$\left[{}^{kj}\widetilde{\mathbf{X}}\right]_E = \begin{bmatrix}\left[{}^k\mathbf{A}_{3,3}\right]_E^{-1}\left[{}^k\mathbf{A}_{1:2,3}\right]_E\frac{1}{2}\sum_j\left(\frac{\partial\, {}^jN}{\partial x_1}\ \left[\mathbf{E}_2\right]_E^T - \sum_j \frac{\partial\, {}^jN}{\partial x_2}\ \left[\mathbf{E}_1\right]_E^T\right)\left[{}^k\mathbf{A}\right]_E\\ \mathbf{0}\end{bmatrix} \tag{50}$$

and so we can write

$$\left[\mathbf{T}^A\right]_E = \begin{bmatrix}\left[{}^1\mathbf{A}\right]_E & \mathbf{0} & \mathbf{0} & \mathbf{0} & \mathbf{0} & \mathbf{0}\\ \left[{}^{11}\widetilde{\mathbf{X}}\right]_E & \left[{}^1\widetilde{\mathbf{A}}\right]_E & \left[{}^{12}\widetilde{\mathbf{X}}\right]_E & \mathbf{0} & \left[{}^{13}\widetilde{\mathbf{X}}\right]_E & \mathbf{0}\\ \mathbf{0} & \mathbf{0} & \left[{}^2\mathbf{A}\right]_E & \mathbf{0} & \mathbf{0} & \mathbf{0}\\ \left[{}^{21}\widetilde{\mathbf{X}}\right]_E & \mathbf{0} & \left[{}^{22}\widetilde{\mathbf{X}}\right]_E & \left[{}^2\widetilde{\mathbf{A}}\right]_E & \left[{}^{23}\widetilde{\mathbf{X}}\right]_E & \mathbf{0}\\ \mathbf{0} & \mathbf{0} & \mathbf{0} & \mathbf{0} & \left[{}^3\mathbf{A}\right]_E & \mathbf{0}\\ \left[{}^{31}\widetilde{\mathbf{X}}\right]_E & \mathbf{0} & \left[{}^{32}\widetilde{\mathbf{X}}\right]_E & \mathbf{0} & \left[{}^{33}\widetilde{\mathbf{X}}\right]_E & \left[{}^3\widetilde{\mathbf{A}}\right]_E\end{bmatrix}_E . \tag{51}$$

At this point, the stiffness matrix $[\mathbf{K}]_A$ still has a rank of only 8. This is now remedied by adding to the diagonal of the element stiffness matrix on the nodal basis an arbitrary torsional stiffness $k_d > 0$ to the drilling degrees of freedom

$$\left[\mathbf{K}_{6,6}\right]_A = k_d,\quad \left[\mathbf{K}_{12,12}\right]_A = k_d,\quad \left[\mathbf{K}_{18,18}\right]_A = k_d\ . \tag{52}$$

We shall leave the choice of the torsional spring constant k_d open for the moment, but we will note that the rank of the element stiffness matrix at this point increases to 11. Note also that the drilling degrees of freedom on the nodal basis are totally decoupled from the flexural response of the element, and the nonzero eigenvalues of the matrix present before the addition of the drilling torsional springs are not affected; the only effect is switching of three zero eigenvalues to nonzero.

Next, the transformation into the global cartesian coordinate system follows.

$$[\mathbf{K}]_G = \left[\mathbf{T}^G\right]_A^T[\mathbf{K}]_A\left[\mathbf{T}^G\right]_A \tag{53}$$

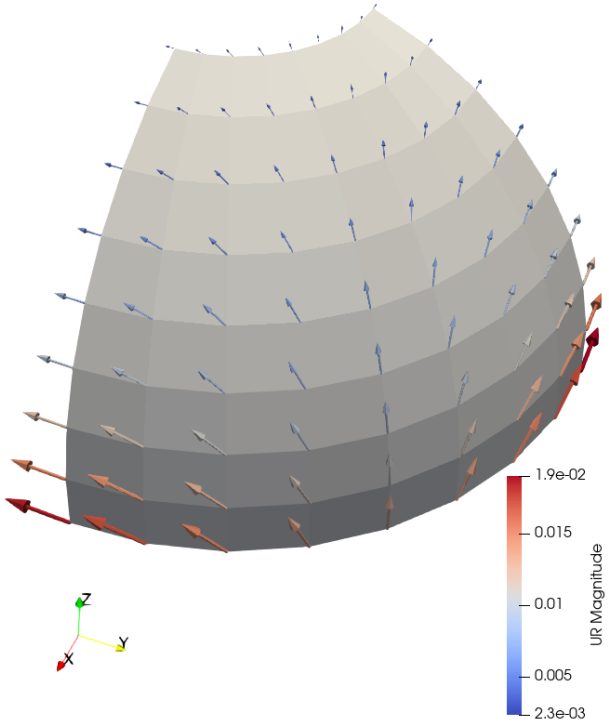

FIGURE 4 Open hemisphere. Resulting nodal rotations visualized as arrows. Note that the rotation vectors are tangent to the surface.

The transformation matrix $\left[\mathbf{T}^G\right]_A$ takes as input a vector in the global cartesian coordinate system (**G**), and outputs a vector in the nodal coordinate basis (**A**):

$$\left[\mathbf{T}^G\right]_A = \begin{bmatrix} \left[{}^1\mathbf{A}\right]_E^T [\mathbf{E}]_G^T & \mathbf{0} & \mathbf{0} & \mathbf{0} & \mathbf{0} & \mathbf{0} \\ \mathbf{0} & \left[{}^1\mathbf{A}\right]_E^T [\mathbf{E}]_G^T & \mathbf{0} & \mathbf{0} & \mathbf{0} & \mathbf{0} \\ \mathbf{0} & \mathbf{0} & \left[{}^2\mathbf{A}\right]_E^T [\mathbf{E}]_G^T & \mathbf{0} & \mathbf{0} & \mathbf{0} \\ \mathbf{0} & \mathbf{0} & \mathbf{0} & \left[{}^2\mathbf{A}\right]_E^T [\mathbf{E}]_G^T & \mathbf{0} & \mathbf{0} \\ \mathbf{0} & \mathbf{0} & \mathbf{0} & \mathbf{0} & \left[{}^3\mathbf{A}\right]_E^T [\mathbf{E}]_G^T & \mathbf{0} \\ \mathbf{0} & \mathbf{0} & \mathbf{0} & \mathbf{0} & \mathbf{0} & \left[{}^3\mathbf{A}\right]_E^T [\mathbf{E}]_G^T \end{bmatrix}_G . \tag{54}$$

The transformations of the stiffness matrix, (51) and (54), lead to a response which is effectively five-degrees of freedom per node internally. However, on the outside the element still has six degrees of freedom per node, and its response is expressed in the global cartesian coordinate system. The nodal basis is not visible on the outside, it is purely on the level of the element.

The internal five-degree of freedom per node character of the formulation is illustrated in Figure 4: the computed rotations for the pinched open hemisphere benchmark are visualized as arrows, which can be seen to be tangent to the spherical surface. In other words, the drilling components of the rotations are practically zero, but they are still computed from the global balance equations that include three rotations per node.

2.2 | Comparison with MacNeal et al. 1998

The transformation (46), (47), has parallels to the transformation proposed by MacNeal et al.[24]. Authors of Reference 24 reacted to the failures reported by Raasch (cited in Knight[25]): Results for the so called Raasch hook problem obtained with Nastran shear-flexible shell elements did not converge, which was explained by the inability of the formulation to transfer correctly twisting moments in curved structures. Reference 24 starts from the inverse of the relation (35), where the matrix $[\mathbf{A}]_E$ is split into two parts, without much motivation or justification, one multiplied by the element rotations, and the other multiplied by the continuum rotations (their equation (6)). The resulting split system of equations is resolved into their equation (12), somewhat

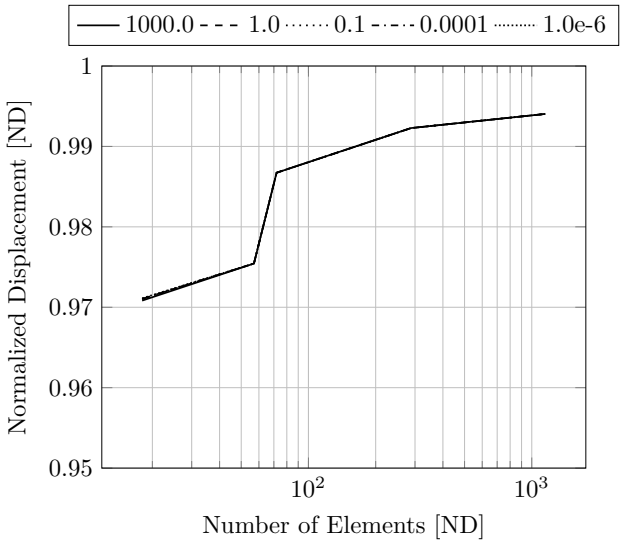

FIGURE 5 Raasch shell. Convergence for five progressively finer meshes with widely varying multiplier of the drilling stiffness. Normalized with the reference solution 5.022 obtained with quadratic serendipity hexahedra and Richardson extrapolation.

resembling our (42). The element drilling rotation is found to depend on the nodal drilling rotation and the continuum rotations out of the plane of the element. In our approach the element drilling rotation is set to zero, and, in the absence of external loading applied to that degree of freedom, the nodal drilling rotation is also zero.

Curiously, the approach of MacNeal et al.[24] produces results quite similar to ours. In other words: it works for the Nastran shell elements. It is then surprising to find that Reference 24 was cited only seven times in the past more than twenty years, and none of the citations appeared to have implemented this technique. A possible reason for this lack of interest may be the relatively impenetrable explanations in Reference 24 (or the lack thereof) of how and why the approach works.

2.3 | Stiffness coefficients for drilling degrees of freedom

So far we have considered a smooth surface, without creases, and without branching. For each node in the mesh, the drilling degree of freedom on the nodal basis is entirely uncoupled from the other degrees of freedom. In equation (52) we introduced arbitrary torsional springs applied to the drilling degrees of freedom. Let us now discuss the numerical value selected for k_d. While the choice may seem arbitrary, it is certainly constrained: very large numbers or very small numbers would be poor choices, because they could easily lead to numerical errors due to round off. Nevertheless, the range in which we can choose k_d is large: Refer to Figure 5, which show the convergence to the correct displacement of the Raasch hook problem for values of the drilling stiffness coefficient that varies across nine orders of magnitude. With the exception of the coarsest mesh, the effect of the drilling stiffness coefficient on the deflection is negligible (the convergence curves visually overlap).

What would be the best value for k_d? From the point of view of the numerical stability of the solution of the coupled system of linear algebraic equations, k_d could be taken for a single element at roughly the same value as (a fraction of?) the other bending stiffness coefficients on the diagonal of the stiffness matrix in the element basis.

$$k_d = \zeta \times \text{mean}_{i=4,5,10,11,16,17} \left(\left[\mathbf{K}_{ii} \right]_E \right) \ . \tag{55}$$

We will discuss the multiplier ζ momentarily.

2.4 | Effect of boundary conditions

Consider the open hemispherical shell benchmark: there are two planes of symmetry. Using these two planes of symmetry, we can reduce the geometry to one quarter of the full shell. Refer to Figure 6.

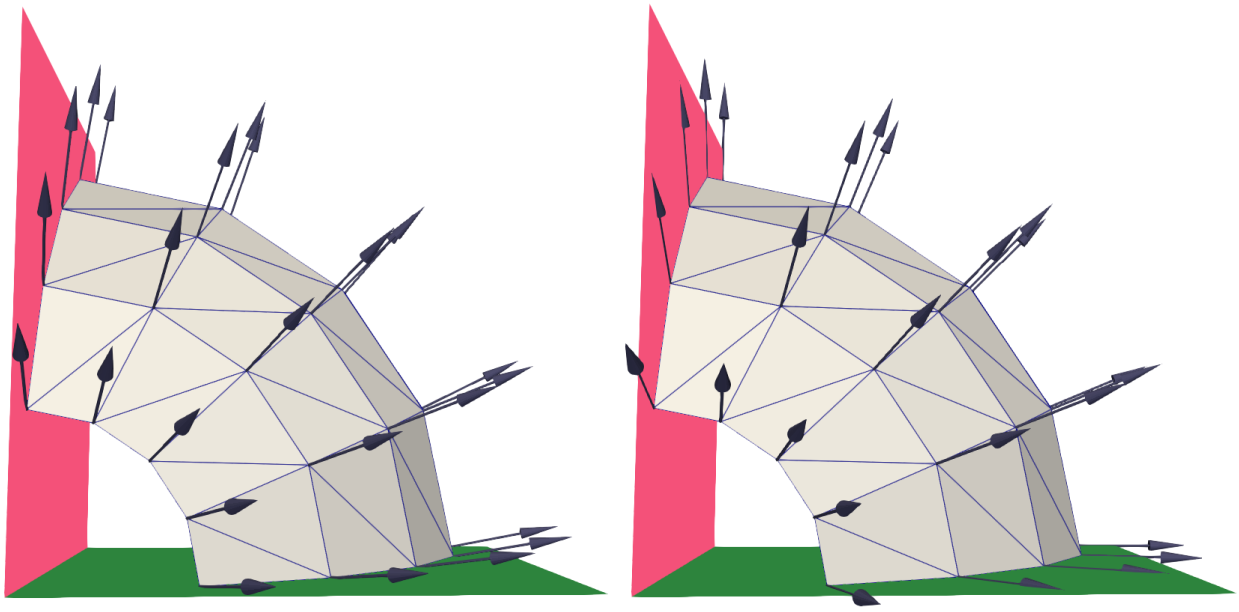

FIGURE 6 Open hemispherical shell. Approximate (on the left) versus exact normals (on the right).

The boundary conditions on the symmetry planes now need to be taken into account. The drilling degrees of freedom are totally independent from each other and from the other degrees of freedom in the system. That is, provided we don't force them to couple with the other rotations. This can happen at the boundaries with prescribed rotations.

Figure 6 illustrates two situations: on the left, the normals have been computed by averaging the normals of the elements connected to a node; we could call this the approximate normals. On the right, the normals have been computed exactly from the geometry of the spherical surface.

Along the boundary curves located in the planes of symmetry, the exact normals lie in the planes of symmetry, whereas the approximate normals have components orthogonal to the planes of symmetry. Since a plane of symmetry only allows rotation about the normal to the plane of symmetry as a free degree of freedom, the bending rotations along the boundary are uncoupled from the drilling rotations when we use the exact normals, but they are coupled to the drilling rotations about the approximate normals. Therefore, if the stiffness coefficient associated with the drilling degrees of freedom are relatively large numbers, this will cause a stiffening of the model. Refinement of the mesh will make the approximate normals approach the plane of symmetry, so this effect does not prevent convergence to the correct result. Figure 7 shows the effect of the magnitude of the drilling stiffness coefficient k_d, which is controlled by the magnitude of the multiplier ζ, on the convergence: on the left for the approximate normals, and on the right for the exact normals. Clearly, using the multiplier $\zeta = 100.0$ significantly reduces the accuracy of a coarse mesh for the approximate normals: the above mentioned stiffening is substantial. Using $\zeta = 1.0$ or smaller has a minimal effect on the solution for the approximate normals. In any case, an arbitrary ζ can be used when the exact normals are adopted, since the results do not depend on it.

The presence of boundaries with support conditions applied to their rotations then necessitates some consideration. We can either

1. provide the exact normals (when available), or adjust the normal at the boundary so that the allowed rotations have no component along the normal, and then use an arbitrary value of the drilling stiffness coefficient; or

2. use the approximate normals with the stiffness coefficient associated with the drilling rotations as defined in equation (55), or a fraction of it.

In this work we adopt the latter approach, with $\zeta = 1.0$.

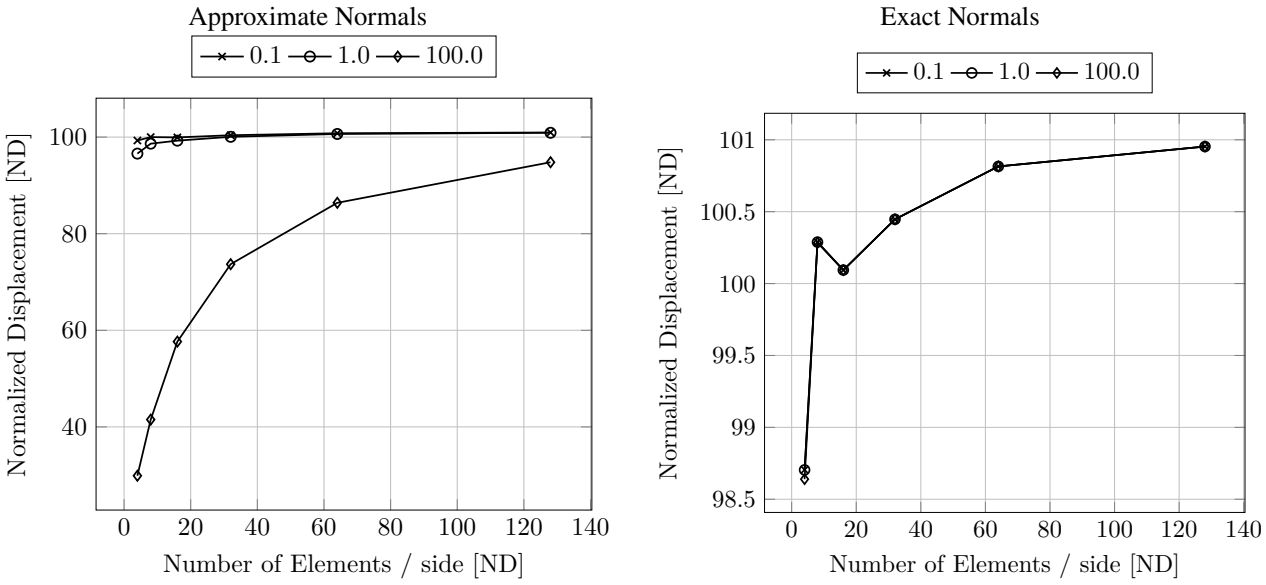

FIGURE 7 Open hemispherical shell benchmark[28]. Normalized deflection under the force for approximate (on the left) versus exact normals (on the right). The drilling stiffness is considered as in Equation (55), with $\zeta = 0.1, 1.0, 100.0$. Results scaled with $100/(0.093)$.

2.5 | Shell with branches or creases

When there is a crease in a shell, the normals at the nodes along the crease cannot be uniquely defined: each surface along the crease has its own normal. Therefore, the drilling degrees of freedom from one side of the crease would interact with the bending degrees of freedom from the other. The drilling stiffness coefficients correspond to springs to the ground, and in general would contribute to an artificial stiffening of the shell. This can be eliminated if we identify the nodes at which the normal is not uniquely defined, and do not attach drilling stiffness coefficients to these degrees of freedom. At the nodes where the normal is not defined, the element calculation can simply substitute the normal to the element surface.

Notice that this also covers the case of a shell with branches: the normals along the junction of the branches are also non-unique, and the same solution as discussed above applies.

2.6 | Dynamics

The mass matrix can be easily constructed as diagonal using a nodal integration rule (three integration points per triangle located at the nodes). The diagonal elements corresponding to translations

$$\left[\mathbf{M}_{ii}\right]_E = \int_A {}^k N^2 t \rho \mathrm{d}A \,, \tag{56}$$

where the degree of freedom i is located at node k, t is the uniform thickness of the element, A is the area of the triangle, and ρ is the mass density, is evaluated as

$$\left[\mathbf{M}_{ii}\right]_E \approx \frac{At\rho}{3} \,. \tag{57}$$

The diagonal elements corresponding to flexural rotations of the nodes can be evaluated using the moment of inertia density[21], again using nodal quadrature, as

$$\left[\mathbf{M}_{ii}\right]_E = \int_A {}^k N^2 \frac{t^3}{12} \rho \mathrm{d}A \approx \frac{At^3\rho}{36} \,, \tag{58}$$

Finally, we need to assign some inertial properties to the drilling degrees of freedom. Leaving these generalized masses as zero would lead to infinite frequencies in the vibration spectrum, not to mention the practical difficulties associated with a singular mass matrix. On the other hand, we do not want to apply excessively large generalized mass coefficients as that would lower

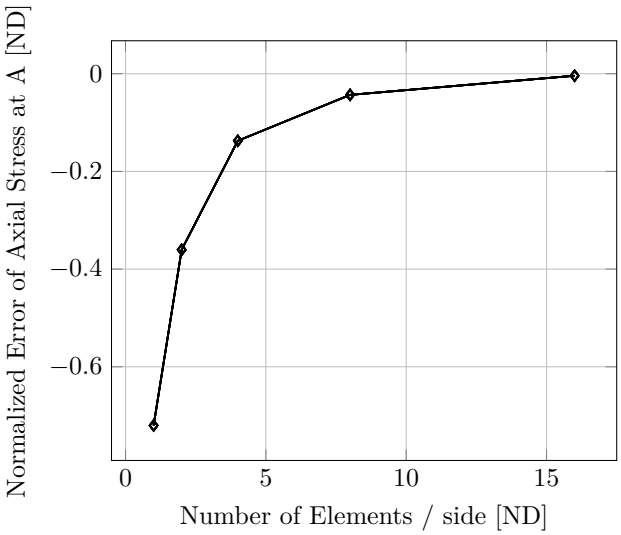

FIGURE 8 Z-section cantilever (LE5). Normalized error of the axial stress at point A (quarter of the distance from the clamped end, at the midsurface, at the free edge of the flange). Results obtained as $(-108 - \sigma_x(A))/(-108)$.

the frequencies corresponding to the drilling degrees of freedom, producing spurious frequencies within the practical range of the frequencies of interest. The reader will recall that we've used as the drilling stiffness coefficient a fraction of the average flexural stiffness coefficient from the diagonal of the stiffness matrix (55). The natural solution then is to use a fraction of the flexural moment of inertia (58) for the generalized mass responding to the drilling degree of freedom. Importantly, the drilling degrees of freedom are uncoupled from each other and from all the other degrees of freedom in the system. Therefore, the mass coefficient for the drilling degree of freedom can be easily adjusted to shift the natural frequencies corresponding to the drilling rotations outside of the frequency range of interest.

3 | NUMERICAL EXAMPLES

A word on the selection of the benchmarks used to test the present formulation: we are certainly aware of the "obstacle course"[29] and the proposed set of benchmarks[28], but from these sets we will only adopt a single test problem, the cylindrical roof (Scordelis-Lo) shell. We will not attempt to establish convergence in the test cases with concentrated loads (the pinched cylinder and the pinched sphere): strictly speaking with a shear flexible shell model no convergence is possible, as the deflection of the target quantity tends to infinity under the force[30]. Hence, we will test the present formulation only with benchmarks in which a distributed loading is applied.

The computations with the present model were implemented in the Julia programming language[31,32], in the framework of the `FinEtoolsFlexStructures.jl` Julia package[33]. The results reported below can be reproduced with the `TestT3FF.jl` Julia package (refer to the data section).

3.1 | Z-section cantilever (LE5)

The Z-section cantilever under torsional loading is a test recommended by the National Agency for Finite Element Methods and Standards (U.K.): Test LE5 from NAFEMS publication TNSB, Rev. 3, "The Standard NAFEMS Benchmarks," October 1990. The target solution is the axial stress, -108 MPa, at the midsurface, at the edge of the flange. Figure 8 shows the convergence to the correct stress value with refinement of the mesh, which starts with 8 element edges along the length, and 1 element edge across the web and across the flanges. The stress values have been obtained by averaging of the element values at the nodes.

Figure 9 shows the rotation vectors computed on the coarsest mesh. Note that the nodes at the longitudinal edges of the flanges are endowed with nodal normals, while the nodes at the creases (corners where the two flat faces of the web and the flange meet) do not use a nodal normal. Consequently, the rotations along the creases do not lie simultaneously in both flat surfaces that meet

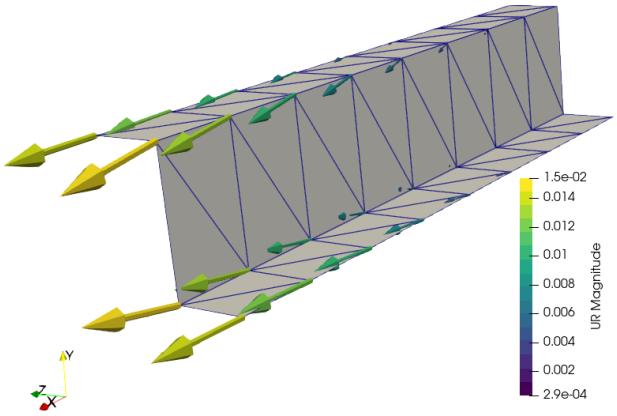

FIGURE 9 Z-section cantilever (LE5). Visualization of the rotation vectors computed on the coarsest mesh.

along the crease. Rather they have a general direction. Conversely, at the nodes with a nodal normal (for the coarsest mesh these are only found along the edges of the flanges), the rotation vectors lie in the tangent plane to the surface.

3.2 | Partially clamped hyperbolic paraboloid shell

The partially clamped hyperbolic paraboloid shell has been proposed as a good test of inextensible bending response in thin shells[34]. Chapelle and Bathe[34] questioned the ability of flat-facet shell models, which includes the present formulation, to "converge to the exact solution of a well defined mathematical model"[34]. As evidence, they presented results of a numerical experiment, deflection of a hyperbolic paraboloid shell under its own weight. The element considered there as a representative of the flat-facet finite element was the DKT plate bending element superimposed with the constant strain membrane element. The membrane response was therefore the same as ours, but we use the isotropic DSG plate element described above, plus the consistent handling of the transfer of bending and twisting moments through the shell.

The numerical experiment was carried out for the thickness to span ratio of 1/1,000. The graph in their Figure 6.2 illustrates failure of the flat-facet shell DKT/CST formulation to converge. We agree that the particular flat-facet shell model studied in Reference 34 may not have been sufficiently robust, but we do think the statement "although facet-shell elements can produce reasonably accurate approximations …, there is evidence that they fail to satisfy the basic convergence properties" is an overgeneralization.

We study this problem with two mesh orientations shown in Figure 10 (the other input parameters are also shown there). Figure 11 shows the normalized displacement produced with the current formulation for three different values of the ratio of the thickness to the span (the span here is 1.0). Clearly, our formulation reliably converges to the correct reference values[35].

Figure 12 demonstrates the convergence for the thickness to span ratio $t/L = 1/1000$ of the present formulation used with the two orientations of the mesh, compared with the most successful MITC triangular element, the MITC3+. Clearly, the MITC3+ element possesses excellent accuracy for coarse meshes, but the rate of convergence in the asymptotic range appears to be the same as for our formulation. The data obtained with the present method is used in Table 1 to estimate the limit value of the deflection with Richardson extrapolation[36]. It is interesting to apply the extrapolation to the MITC3+ data as well: the downward deflection estimated from the data from Reference 37, i.e. -6.440048×10^{-3}, is 0.7186% larger in magnitude than the reference value.

3.3 | Scordelis-Lo roof

The Scordelis-Lo roof is one of the original obstacle course benchmarks[28]. The cylindrical shell problem parameters considered here are (in consistent English units, with lengths in feet): length 50.0, radius 25.0, thickness 0.25, Young's modulus 4.32×10^8, Poisson ratio 0.0, gravity load per unit area 90.0.

Reference 28 proposed deflection at the midpoint of the straight edge of the cylindrical shell of -0.3024, but there is evidence that for shell models without shear deformation the deflection is close to -0.3006[38,39]. Personal communication[40] has provided

TABLE 1 Partially clamped hyperbolic paraboloid shell. Thickness to span ratio $t/L = 1/1000$. Estimated limit value of the deflection (positive relative difference with respect to -6.3941×10^{-3} means the downward deflection is larger in magnitude then the reference value).

Mesh orientation	# element edges	Result$\times 10^3$	Estimated limit (relative difference)
(a)	96	−6.220867	-6.408738×10^{-3} (0.2289%)
	192	−6.325592	
	384	−6.371940	
(b)	96	−6.310121	-6.402151×10^{-3} (0.1259%)
	192	−6.363234	
	384	−6.385700	

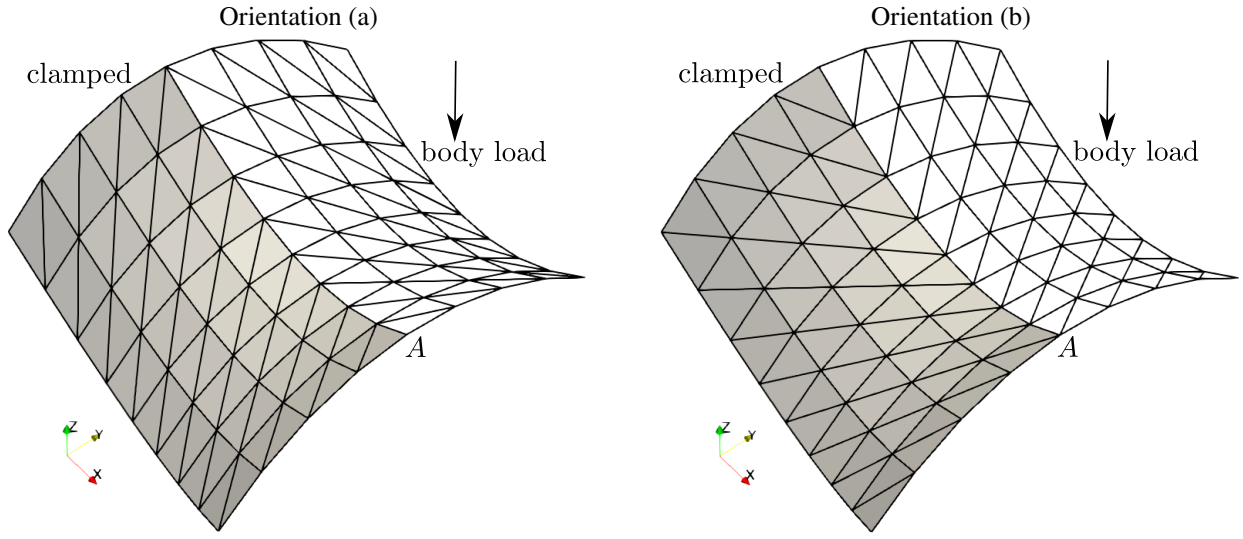

FIGURE 10 Partially clamped hyperbolic paraboloid shell. Meshes of orientation (a) and (b), with 8 element edges. The modeled half of the structure is shown in solid color; the wireframe rendering on the right represents the omitted part of the shell. Surface formula $Z = -X^2 + Y^2$, for $-1/2 \le X \le +1/2$ and $-1/2 \le Y \le +1/2$. $E = 2 \times 10^{11}$, $\nu = 0.3$, vertical body load 8,000/unit volume. Target value: Z deflection at point A.

TABLE 2 Scordelis-Lo roof. Computed deflection at the midpoint of the straight edge.

Number of element edges	4	8	16	32	64
Result	-0.201457	-0.236826	-0.258812	-0.288552	-0.297828

a more precise number of -0.300592437, which is used in Figure 13 to (re)normalize results from the literature in comparison with our own results.

The computed deflections are summarized in Table 2 for five regular meshes obtained by refinement with the factor of two. Extrapolating using the Richardson method[36] from the last three results in Table 2 results in -0.301334. This is slightly larger deflection than -0.300592437 reported for Kirchhoff-Love shells[40], potentially accounting for transverse shear flexibility (compare with -0.3020 reported by Kiendl et al.[41]).

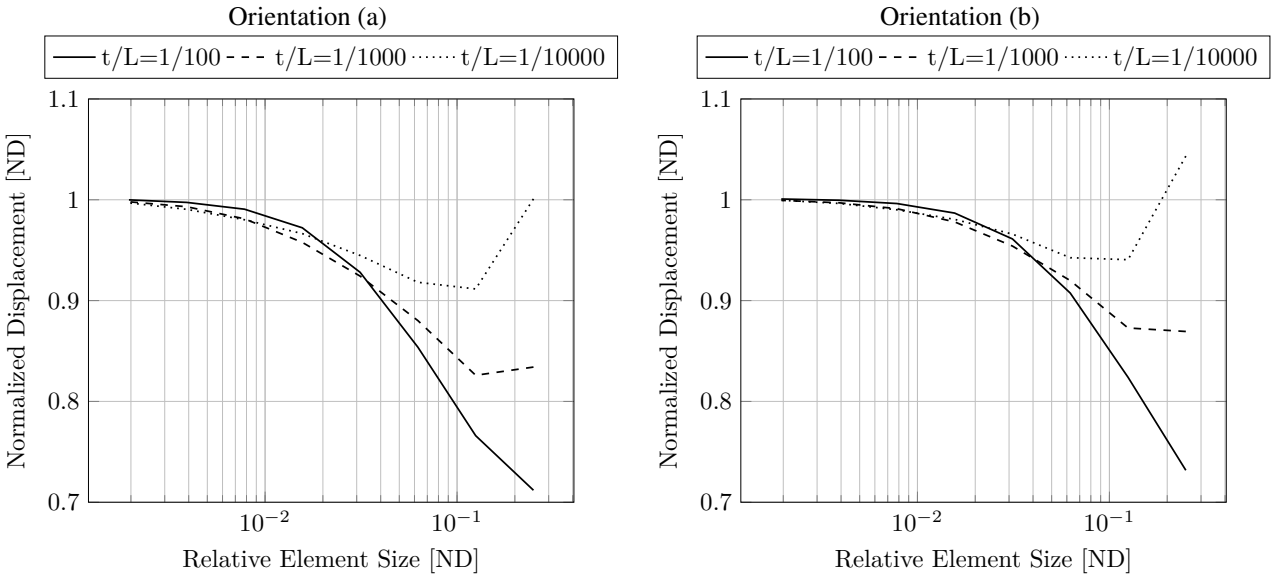

FIGURE 11 Partially clamped hyperbolic paraboloid shell. Convergence of the deflection for three different thicknesses. Mesh orientation (a) and (b). The source of the target data: Reference 35, thickness to span $t/L = 1/100$: deflection -9.3355×10^{-5}, 1/1000: deflection -6.3941×10^{-3}, 1/10,000: deflection -5.2988×10^{-1} .

3.4 | Hyperboloid of revolution shell with $\cos(2\varphi)$-distributed pressure

These tests have been proposed by Hiller and Bathe[44]. The structure is a free or clamped single-sheet hyperboloid of revolution. It is loaded with a normal pressure with circumferential variation according to $\cos(2\varphi)$. Three planes of symmetry are used to reduce the geometry to one eighth of the full shell, compare with Figure 14.

The goal is to study a non-trivial shell, with nonzero Gaussian curvature, either to explore bending-dominated response (when the edges are free), or to subject the shell to membrane-dominated response and a boundary layer (when the edges are clamped).

The convergence of the strain energy is studied using the definition of the relative approximate error

$$e_{E,j} = \frac{E_{h,j+1} - E_{h,j}}{E_{h,n}} \,, \tag{59}$$

where $E_{h,j}$ is the strain energy for the element size h_j, and $E_{h,n}$ is the strain energy computed for the finest mesh. In case the mesh is irregular (distorted), as for instance in Figure 14, the element size is defined as the element size for a mesh of regular shapes with the same number of elements.

Figure 15 shows the convergence of the relative strain energy error (59) for the free hyperboloid of revolution for four values of the element thickness. Here the half length of the shell is $L = 1$, and hence the ratio of the thickness to the length, t/L, takes on values of $1/100$, $1/1,000$, $1/10,000$, and $1/100,000$. Two meshes are used: a regular one, and a strongly distorted mesh (Figure 14). Neither the thickness, nor the distortion of the mesh play a very strong role, but the convergence rate deteriorates somewhat when the thickness is reduced.

Figure 16 shows an analogous plot for the clamped case: The circular edges are clamped, which produces a strong boundary layer. The boundary layer was identified in Reference 44 as a possible source of reduced convergence rate. The convergence rate does not seem to be affected very strongly, at least for practical thickness to length ratios, but the absolute error certainly increases with the decrease in shell thickness. The effect of the distortion of the mesh is quite minor: it would seem that the present formulation is quite resistant to element shape distortion.

3.5 | Cylindrical container with stiffeners

In this example we consider a structure representative of industrial applications. The structure represents an empty container with spherical caps, two stiffeners, and edge beams. Figure 17 shows the geometry with the generating section included: Clearly, this example tests the ability to represent creases in the surface, and junctions with more than two shell faces joined along a

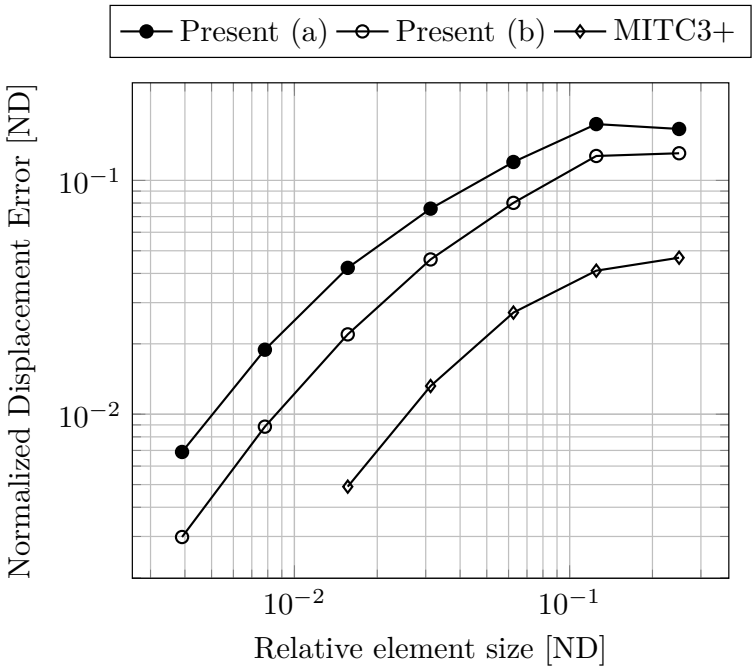

FIGURE 12 Partially clamped hyperbolic paraboloid shell. Thickness 1/1000. Comparison of the present element with two mesh orientations, (a) and (b), and the MITC3+ elements[37]. Results scaled with $100/(-6.3941 \times 10^{-3})$.

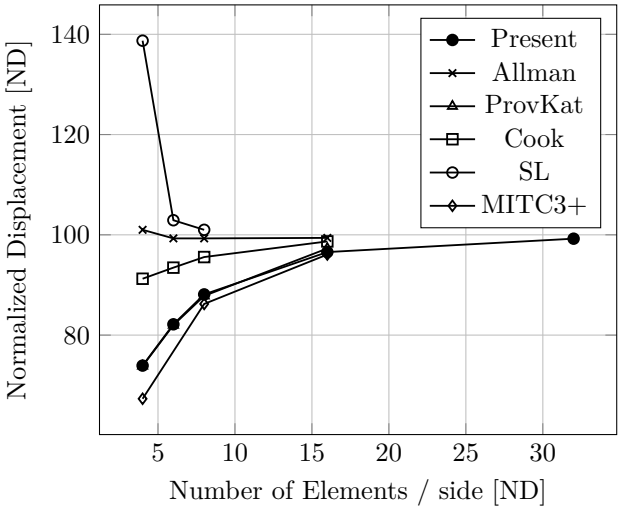

FIGURE 13 Scordelis-Lo roof. Regular mesh, with equal number of element edges per side of the modelled quarter of the shell in both directions. Comparison with other triangular elements[23]: Allman[10], ProvKat[42], Cook[11], SL[43], MITC3+[37]. Results scaled with $(-100/0.300592437)$.

curve (branched shells). The material is mild steel with $E = 200,000$ MPa, $\nu = 0.3$, $\rho = 7850\,\mathrm{kg/m^3}$. A shop drawing of the generating section is given in Section A.

We solve the free vibration problem, requesting 40 natural frequencies. In Table 3 we compare the computed frequencies using our approach and some of the Abaqus quadrilateral and triangular elements (S4: fully integrated variant of the MITC quadrilateral element, S4R: uniform underintegration for the quadrilateral with stabilization, S3: MITC quadrilateral element degenerated into a triangle, STRI3: triangular thin shell specialist with a discrete Kirchhoff constraint)[45]. Quadrilateral meshes: 121,987 nodes, 122,599 elements. Triangular meshes: 113,080 nodes, 226,144 elements. There are six rigid body displacement

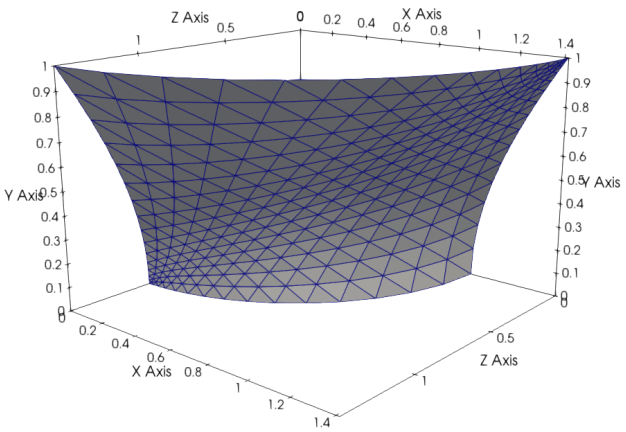

FIGURE 14 Clamped hyperboloid of revolution shell. Distorted mesh with 16 edges on the side.

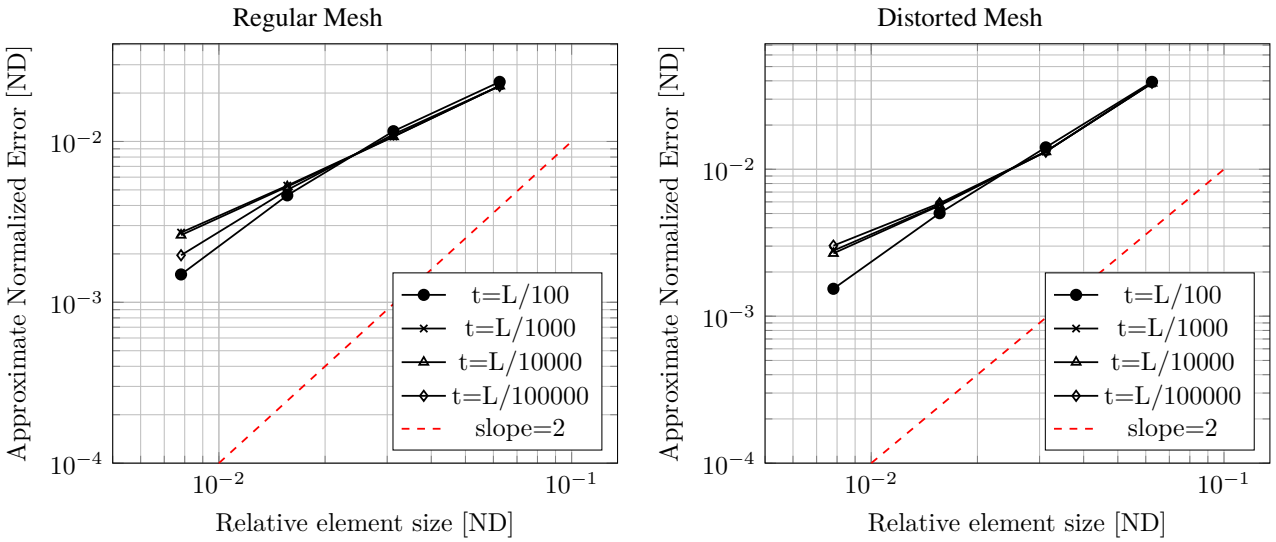

FIGURE 15 Free hyperboloid of revolution shell loaded with $\cos(2\varphi)$ pressure. Convergence of the normalized approximate strain energy error.

modes (with zero natural frequencies), and the 10 reported non-zero frequencies agree very well. The eigenvalue (free vibration) problem solutions were in our simulations obtained with Arpack[46] (accessed through the Julia package `Arpack.jl`[47]). This matches the Lanczos eigenvalue solver implemented in the commercial software.

We wish to demonstrate here the computational efficiency of the present approach. The absolute numbers are not of interest, we shall focus on relative timings. The present model and the simulations with Abaqus were exercised on the same machine, serially, which means that no explicit parallelization was employed (but the linear algebra library might have executed parts of the calculations in parallel using threads). The measurements are summarized in Table 4. The solution of the eigenvalue problem took roughly the same time for the models based on triangular meshes, and the same time for the models based on quadrilateral meshes. The time increased for the quadrilateral meshes because the number of nodes was larger. The preprocessing and post processing includes everything except the solution of the eigenvalue problem, and in particular it comprises the reading of the mesh, construction of the linear algebra objects (the stiffness and the mass matrix), any bookkeeping, and after the solution of the eigenvalue problem is obtained, writing out of the post processing files. The computation with the present model executed in Julia from a cold start: this means that the code needed to be compiled before its first use. This is significant, since the compilation time was on the order of 14 seconds. Therefore, if the compilation time was subtracted, the pre- and post processing with our model would have executed in 13 seconds. Hence, quite competitive. The present model identified the creases and the

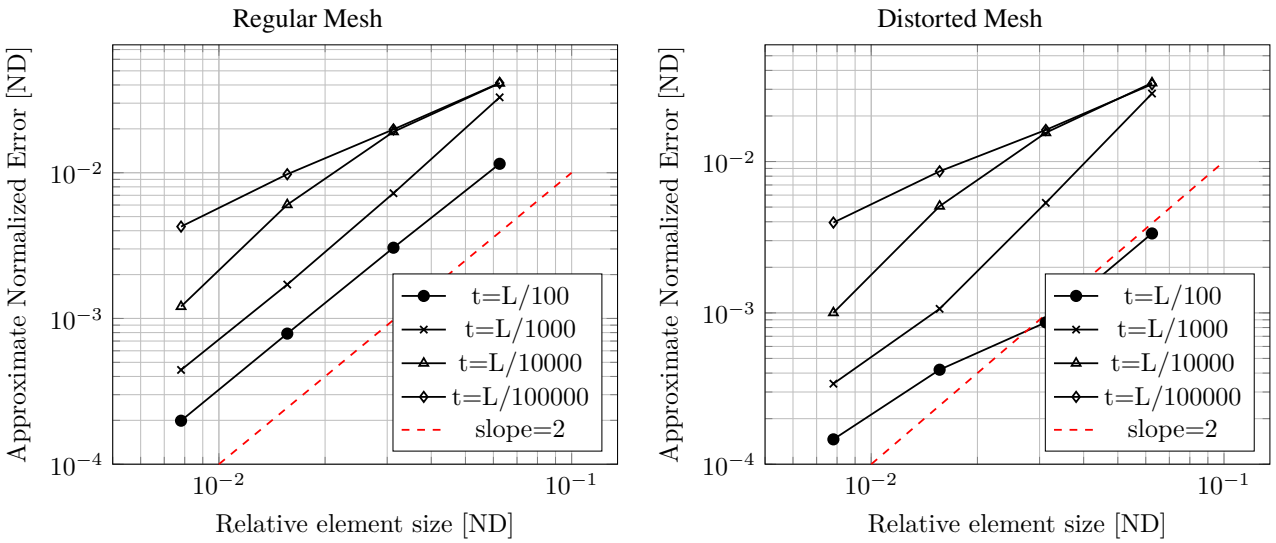

FIGURE 16 Clamped hyperboloid of revolution shell loaded with $\cos(2\varphi)$ pressure. Convergence of the normalized approximate strain energy error.

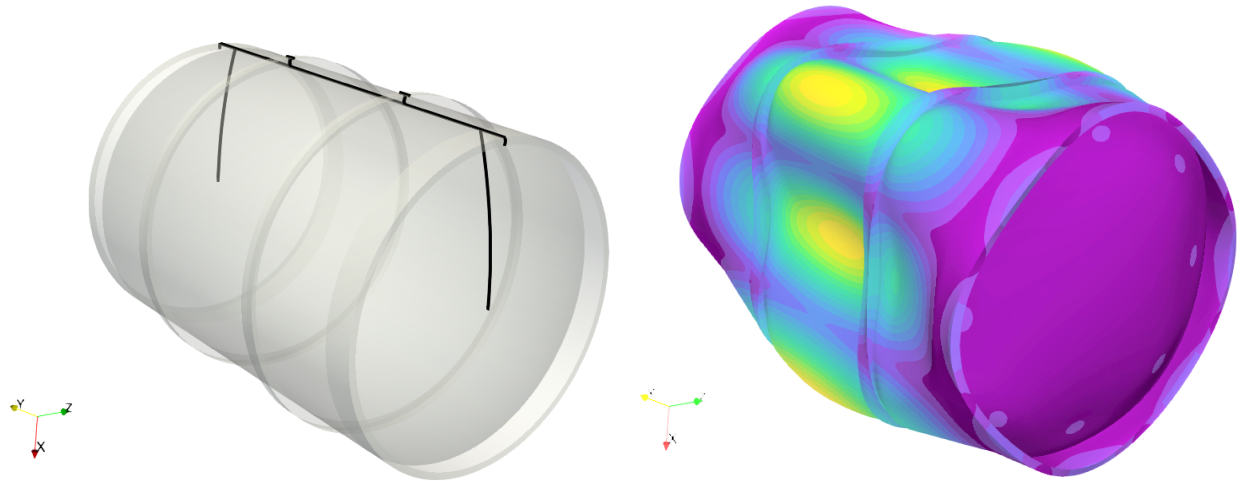

FIGURE 17 Cylindrical container with stiffeners. On the left: Geometry with the generating section. Note the T-shaped stiffeners, and the rim stiffener. On the right: mode shape 7 for the (fundamental) natural frequency of 231.40 Hz.

branching curves in 1.3 seconds, computed the stiffness matrix in 5.5 seconds, and computed the mass matrix in 2.8 seconds. These times include the compilation of the code.

CONCLUSIONS

A flat-facet triangular finite element for shear-deformable shell structures was presented. The constant-strain membrane triangle was combined with a discrete shear gap plate element. Two techniques of enforcing isotropic transverse shear response were devised and compared with approaches from the literature.

The element uses five degrees of freedom per node (three translations and two flexural rotations), as the drilling rotation at the element level is meaningless. A transformation between the element cartesian frame and the global cartesian coordinate system via an intermediate basis at the nodes was formulated. The intermediate basis at the nodes was based on uniquely defined

TABLE 3 Cylindrical container with stiffeners. Natural frequencies. The first six frequencies are rigid body modes. The listed frequencies come in pairs.

	Natural Frequencies [Hz]				
Formulation	Fundamental (7, 8)	(9, 10)	(11, 12)	(13, 14)	(15, 16)
S4	230.67	237.89	250.38	252.33	259.20
S4R	230.18	237.69	250.26	252.17	258.60
S3	232.12	238.50	250.72	252.79	260.69
STRI3	231.48	238.19	250.09	252.19	260.12
Present	231.40	238.16	250.09	252.18	260.02

TABLE 4 Cylindrical container with stiffeners. Timings.

Formulation	Total time [s]	Eigenvalue problem [s]	Pre- and post-processing [s]
S4	140	121	19
S4R	133	121	12
S3	120	101	19
STRI3	119	99	20
Present	133	106	27

directions at nodes where the shell was smooth. The transformation totally decoupled the global drilling degrees of freedom from the elementwise flexural deformations. The global drilling degrees of freedom then end up independent of each other, and decoupled from the other degrees of freedom in the system. Hence, an arbitrary stiffness coefficient could be applied to the drilling degrees of freedom. Its value is theoretically immaterial, but practically one would wish to control the magnitude to ensure good conditioning of the global stiffness matrix. Therefore, we set the drilling stiffness to be similar to the flexural stiffness coefficients.

At nodes where the shell either branches, or where it has a crease, no unique normal can be defined. The normal assumed for the element-to-global transformations could then be taken to be that of the attached elements themselves, and no drilling stiffness was applied at such nodes. Folded shells and shells with branches present therefore no problems.

Numerical examples were used to illustrate the performance with particular attention to robustness of the treatment of the drilling degrees of freedom, sensitivity to element shape, and susceptibility to shear locking. The present formulation showed a satisfactory insensitivity to poor aspect ratios, and was found insensitive to shear locking.

Although only linear static and dynamic problems were addressed, and the material of the shell was assumed homogeneous and isotropic, extensions in multiple directions are possible: The material need not be isotropic, and layered shells may be incorporated with classical plate theory of lamination. Firm control over the drilling degrees of freedom means that the model may be suitable for applications in explicit dynamics analyses: we can avoid large frequencies associated with the drilling degrees of freedom. Inelastic response and geometrical nonlinearity are further areas of future research.

ACKNOWLEDGEMENTS

Josef Kiendl kindly provided some data to assist with the analysis of the Scordelis-Lo roof structure.

FINANCIAL DISCLOSURE

None reported.

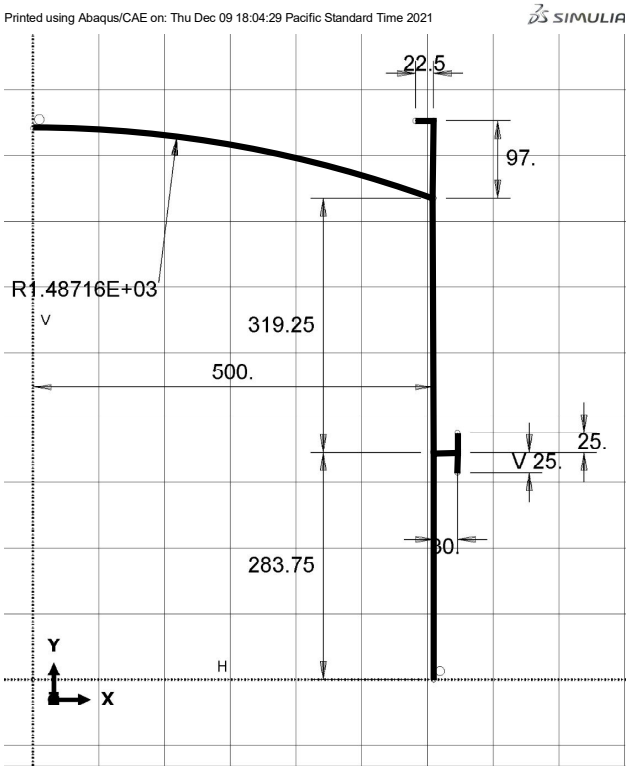

FIGURE A1 Cylindrical container with stiffeners. Sketch of one half of the generating section (the other half is symmetric with respect to the horizontal line at the bottom). All dimensions are given in millimeters. Thickness of the material of the walls is 2 mm.

CONFLICT OF INTEREST

The authors declare no potential conflict of interests.

DATA AVAILABILITY

The source code and data used to produce the results in this paper are freely available in the repository https://github.com/PetrKryslUCSD/TestT3FF.jl. The source code of the finite element formulation is available in the repository https://github.com/PetrKryslUCSD/FinEtoolsFlexStructures.jl.

APPENDIX

A CONTAINER WITH STIFFENERS

References

1. Schollhammer D, Fries TP. Reissner-Mindlin shell theory based on tangential differential calculus. *Computer Methods in Applied Mechanics and Engineering* 2019; 352: 172-188. doi: 10.1016/j.cma.2019.04.018

2. Zou Z, Hughes TJR, Scott MA, Sauer RA, Savitha EJ. Galerkin formulations of isogeometric shell analysis: Alleviating locking with Greville quadratures and higher-order elements. *Computer Methods in Applied Mechanics and Engineering* 2021; 380: 113757. doi: https://doi.org/10.1016/j.cma.2021.113757

3. Sangtarash H, Arab HG, Sohrabi MR, Ghasemi MR. A high-performance four-node flat shell element with drilling degrees of freedom. *Engineering with Computers* 2021; 37(4): 2837-2852. doi: 10.1007/s00366-020-00974-4

4. Yang HTY, Saigal S, Masud A, Kapania RK. A survey of recent shell finite elements. *International Journal for Numerical Methods in Engineering* 2000; 47(1-3): 101-127.

5. Reddy JN, Arciniega RA. Shear deformation plate and shell theories: From Stavsky to present. *Mechanics of Advanced Materials and Structures* 2004; 11(6): 535-582. doi: 10.1080/15376490490452777

6. Irfan S, Siddiqui F. A review of recent advancements in finite element formulation for sandwich plates. *Chinese Journal of Aeronautics* 2019; 32(4): 785-798. doi: 10.1016/j.cja.2018.11.011

7. Lavrencic M, Brank B. Hybrid-Mixed Low-Order Finite Elements for Geometrically Exact Shell Models: Overview and Comparison. *Archives of Computational Methods in Engineering* 2021; 28(5): 3917-3951. doi: 10.1007/s11831-021-09537-2

8. Allman DJ. Analysis Of General Shells By Flat Facet Finite-Element Approximation. *Aeronautical Journal* 1991; 95(946): 194-203.

9. Bletzinger KU, Bischoff M, Ramm E. A unified approach for shear-locking-free triangular and rectangular shell finite elements. *Computers & Structures* 2000; 75(3): 321-334. doi: https://doi.org/10.1016/S0045-7949(99)00140-6

10. Allman DJ. A Basic Flat Facet Finite-Element For The Analysis Of General Shells. *International Journal for Numerical Methods in Engineering* 1994; 37(1): 19-35. doi: 10.1002/nme.1620370103

11. Cook RD. Further Development Of A 3-Node Triangular Shell Element. *International Journal for Numerical Methods in Engineering* 1993; 36(8): 1413-1425. doi: 10.1002/nme.1620360809

12. Winkler R, Plakomytis D. A New Shell Finite Element With Drilling Degrees Of Freedom And Its Relation To Existing Formulations. In: Papadrakakis M, Papadopoulos V, Stefanou G, Plevris V., eds. *ECCOMAS Congress 2016, VII European Congress on Computational Methods in Applied Sciences and Engineering*.

13. Choi JH, Lee BC. Rotation-free triangular shell element using node-based smoothed finite element method. *International Journal for Numerical Methods in Engineering* 2018; 116(6): 359-379. doi: 10.1002/nme.5928

14. Ludwig T, Hühne C, De Lorenzis L. Rotation-free Bernstein–Bézier elements for thin plates and shells — development and validation. *Computer Methods in Applied Mechanics and Engineering* 2019; 348: 500-534. doi: 10.1016/j.cma.2019.01.039

15. Cui XY, Liu GR, Li GY, Zhang GY, Zheng G. Analysis of plates and shells using an edge-based smoothed finite element method. *Computational Mechanics* 2010; 45(2-3): 141-156. doi: 10.1007/s00466-009-0429-9

16. Nguyen-Thoi T, Phung-Van P, Nguyen-Xuan H, Thai-Hoang C. A cell-based smoothed discrete shear gap method using triangular elements for static and free vibration analyses of Reissner-Mindlin plates. *International Journal for Numerical Methods in Engineering* 2012; 91(7): 705-741. doi: 10.1002/nme.4289

17. Cui XY, Tian L. A Central Point-Based Discrete Shear Gap Method for Plates and Shells Analysis Using Triangular Elements. *International Journal of Applied Mechanics* 2017; 9(4). doi: 10.1142/s1758825117500557

18. Talaslidis D, Wempner GA. The Linear Isoparametric Triangular Element - Theory And Application. *Computer Methods in Applied Mechanics and Engineering* 1993; 103(3): 375-397. doi: 10.1016/0045-7825(93)90129-l

19. Lyly M, Stenberg R, Vihinen T. A stable bilinear element for Reissner–Mindlin plate model. *Computer Methods in Applied Mechanics and Engineering* 1993; 110: 343-357. doi: 10.1016/0045-7825(93)90214-I

20. Bischoff M, Bletzinger KU. Improving stability and accuracy of Reissner-Mindlin plate finite elements via algebraic subgrid scale stabilization. *Computer Methods in Applied Mechanics and Engineering* 2004; 193(15-16): 1517-1528. doi: 10.1016/j.cma.2003.12.036

21. Zienkiewicz OC, Taylor RL, Fox D. *The Finite Element Method for Solid and Structural Mechanics: Seventh Edition*. The Finite Element Method for Solid and Structural Mechanics: Seventh Edition . 2013

22. Providas E, Kattis MA. An assessment of two fundamental flat triangular shell elements with drilling rotations. *Computers & Structures* 2000; 77(2): 129-139. doi: 10.1016/s0045-7949(99)00215-1

23. Sangtarash H, Arab HG, Sohrabi MR, Ghasemi MR. An efficient three-node triangular Mindlin-Reissner flat shell element. *Journal of the Brazilian Society of Mechanical Sciences and Engineering* 2020; 42(6). doi: 10.1007/s40430-020-02420-4

24. MacNeal RH, Wilson CT, Harder RL, Hoff CC. The treatment of shell normals in finite element analysis. *Finite Elements in Analysis and Design* 1998; 30(3): 235-242. doi: 10.1016/s0168-874x(98)00035-3

25. Knight NF. Raasch challenge for shell elements. *Aiaa Journal* 1997; 35(2): 375-381. doi: 10.2514/2.104

26. Schoop H, Hornig J, Wenzel T. Remarks on Raasch's Hook. *TECHNISCHE MECHANIK* 2002; 22(4): 259-270.

27. Shang Y, Cen S, Li CF. A 4-node quadrilateral flat shell element formulated by the shape-free HDF plate and HSF membrane elements. *Engineering Computations* 2016; 33(3): 713-741. doi: 10.1108/ec-04-2015-0102

28. Macneal RH, Harder RL. A proposed standard set of problems to test finite element accuracy. *Finite Elements in Analysis and Design* 1985; 1(1): 3-20. doi: 10.1016/0168-874X(85)90003-4

29. Belytschko T, Stolarski H, Liu WK, Carpenter N, Ong JSJ. Stress Projection For Membrane And Shear Locking In Shell Finite-Elements. *Computer Methods in Applied Mechanics and Engineering* 1985; 51(1-3): 221-258. doi: 10.1016/0045-7825(85)90035-0

30. Babuska I, Oden J. Benchmark Computation: What is the Purpose and Meaning?. *IACM Bulletin* 1992; 7(4): 83-84.

31. The Julia Project . The Julia Programming Language. https://julialang.org/; Accessed 03/13/2021.

32. Bezanson J, Edelman A, Karpinski S, Shah VB. Julia: A fresh approach to numerical computing. *SIAM review* 2017; 59(1): 65–98.

33. Petr Krysl . FinEtoolsFlexStructures: Finite Element tools for flexible beams and shells in Julia. https://github.com/PetrKryslUCSD/FinEtoolsFlexStructures.jl; Accessed 12/13/2021.

34. Chapelle D, Bathe KJ. *The Finite Element Analysis of Shells — Fundamentals* ch. Displacement-Based Shell Finite Elements: 171-205; Berlin, Heidelberg: Springer Berlin Heidelberg . 2003

35. Bathe KJ, Iosilevich A, Chapelle D. An evaluation of the MITC shell elements. *Computers & Structures* 2000; 75(1): 1-30. doi: 10.1016/s0045-7949(99)00214-x

36. Krysl P. *Finite Element Modeling with Abaqus and Python for Thermal and Stress Analysis*. Pressure Cooker Press, https://doi.org/10.5281/zenodo.5778216. 3 ed. 2021.

37. Ko Y, Lee Y, Lee PS, Bathe KJ. Performance of the MITC3+ and MITC4+ shell elements in widely-used benchmark problems. *Computers & Structures* 2017; 193: 187-206. doi: 10.1016/j.compstruc.2017.08.003

38. Kiendl J, Bletzinger KU, Linhard J, Wuchner R. Isogeometric shell analysis with Kirchhoff-Love elements. *Computer Methods in Applied Mechanics and Engineering* 2009; 198(49-52): 3902-3914. doi: 10.1016/j.cma.2009.08.013

39. Coox L, Maurin F, Greco F, Deckers E, Vandepitte D, Desmet W. A flexible approach for coupling NURBS patches in rotationless isogeometric analysis of Kirchhoff–Love shells. *Computer Methods in Applied Mechanics and Engineering* 2017; 325: 505-531. doi: https://doi.org/10.1016/j.cma.2017.07.022

40. Kiendl J. Personal Communication. 2021.

41. Kiendl J, Marino E, De Lorenzis L. Isogeometric collocation for the Reissner-Mindlin shell problem. *Computer Methods in Applied Mechanics and Engineering* 2017; 325: 645-665. doi: 10.1016/j.cma.2017.07.023

42. Providas E, Kattis MA. An assessment of two fundamental flat triangular shell elements with drilling rotations. *Computers & Structures* 2000; 77(2): 129-139. doi: 10.1016/s0045-7949(99)00215-1

43. Shin CM, Lee BC. Development of a strain-smoothed three-node triangular flat shell element with drilling degrees of freedom. *Finite Elements in Analysis and Design* 2014; 86: 71-80. doi: 10.1016/j.finel.2014.04.002

44. Hiller JF, Bathe KJ. Measuring convergence of mixed finite element discretizations: an application to shell structures. *Computers & Structures* 2003; 81(8-11): 639-654. doi: 10.1016/s0045-7949(03)00010-5

45. Dassault Systèmes *Abaqus Theory Manual*. version 6.14 ed. 2014.

46. ARPACK developers . Arpack official website. https://www.caam.rice.edu/software/ARPACK/; Accessed 04/11/2019.

47. Julia Linear algebra development team . The Arnoldi eigenvalue problem solvers Arpack.jl. https://github.com/JuliaLinearAlgebra/Arpack.jl; Accessed 04/11/2019.